Chemical Science

ROYAL SOCIETY OF CHEMISTRY

EDGE ARTICLE

View Article Online
View Journal | View Issue

Cite this: *Chem. Sci.*, 2026, **17**, 6773

All publication charges for this article have been paid for by the Royal Society of Chemistry

NaCl interphase enables stable $Na_{2.85}Sb_{0.95}W_{0.05}S_{3.9}Cl_{0.1}$-based all-solid-state sodium batteries

Zhanyou Feng,[ac] Liang Zhu,[a] Enbo Qin,[a] Ziman Weng,[a] Jinghua Wu,[ab] Yong Li*[ab] and Xiayin Yao*[ab]

Received 23rd November 2025
Accepted 24th January 2026

DOI: 10.1039/d5sc09154c

rsc.li/chemical-science

All-solid-state sodium (Na) batteries (ASSSBs) have attracted considerable attention due to their inherent safety and low cost. Developing sodium sulfide electrolytes with high Na^+ ionic conductivity and excellent stability in contact with sodium metal anodes is crucial to realize high-performance ASSSBs. Herein, a tungsten (W) and chlorine (Cl) co-doped $Na_{2.85}Sb_{0.95}W_{0.05}S_{3.9}Cl_{0.1}$ solid electrolyte is effectively prepared through melt-quenching combined with a subsequent annealing process. Through W–Cl co-doping, Na vacancies are introduced into the Na_3SbS_4 electrolyte, thereby enhancing the ionic conductivity from 0.92 mS cm^{-1} to 12.66 mS cm^{-1}. Meanwhile, the *in situ* formed NaCl-based electronically insulating interphase layer between $Na_{2.85}Sb_{0.95}W_{0.05}S_{3.9}Cl_{0.1}$ and the sodium metal effectively suppresses interfacial side reactions and improves interfacial stability. The obtained Na/$Na_{2.85}Sb_{0.95}W_{0.05}S_{3.9}Cl_{0.1}$/Na symmetric cell demonstrates stable cycling over 800 h at 0.05 mA cm^{-2}. Moreover, the TiS_2/$Na_{2.85}Sb_{0.95}W_{0.05}S_{3.9}Cl_{0.1}$/Na ASSSB realizes an initial charge capacity of 142.2 mAh g^{-1} at 0.1C, maintaining a capacity retention of 81.6% after 100 cycles. This work presents a viable approach for designing sodium sulfide electrolytes that combine high ionic conductivity with superior stability with a sodium anode.

1. Introduction

Sodium-ion batteries have attracted significant attention due to the abundance of sodium resources and their low cost.[1–3] However, conventional sodium-ion batteries that rely on organic liquid electrolytes raise safety concerns, including the risk of electrolyte leakage and flammability.[4–6] All-solid-state sodium batteries (ASSSBs) exhibit enhanced safety because of the replacement of liquid electrolytes with solid electrolytes. Moreover, the use of high specific capacity sodium metal as an anode holds promise for significantly improving a battery's energy density.[7–9]

Sodium sulfide electrolytes exhibit excellent mechanical flexibility, which facilitates robust interfacial adhesion with active materials *via* cold-pressing techniques, thereby demonstrating great potential for application in ASSSBs.[10,11] As a representative sodium sulfide electrolyte, Na_3SbS_4 exhibits excellent air stability along with a relatively high ionic conductivity reaching 10^{-3} S cm^{-1}.[12] Zhang *et al.* synthesized a tetragonal-phase Na_3SbS_4 solid electrolyte and found that only 80% of the Na2 sites were occupied by Na^+ ions, with the remaining 20% being vacancies. The as-prepared Na_3SbS_4 demonstrated a room-temperature ionic conductivity of 3 mS cm^{-1}, indicating that sodium vacancies facilitate Na^+ transport within the solid electrolyte.[13] Tsuji *et al.* synthesized a Mo^{6+}-doped Na_3SbS_4 solid electrolyte by substituting Sb^{5+} with Mo^{6+}. Based on the principle of charge compensation, this aliovalent substitution introduced Na^+ vacancies and replaced SbS_4^{3-} structural units with MoS_4^{2-}, resulting in an improved ionic conductivity of 3.9 mS cm^{-1} for $Na_{2.88}Sb_{0.88}Mo_{0.12}S_4$.[14] Similarly, Hayashi *et al.* reported that replacing Sb^{5+} with W^{6+} resulted in the formation of Na^+ vacancies and the substitution of SbS_4^{3-} units with WS_4^{2-}, leading to a significantly enhanced ionic conductivity of 32 mS cm^{-1} for ball-milled $Na_{2.88}Sb_{0.88}W_{0.12}S_4$.[15]

Recently, Weng *et al.* synthesized W^{6+}-doped $Na_{2.95}Sb_{0.95}W_{0.05}S_4$ solid electrolytes *via* a melt-quenching method, which achieved an impressive ionic conductivity of 10.3 mS cm^{-1}.[16] However, despite the improved conductivity, W^{6+} doping was found to compromise interfacial stability due to the easy reduction of W^{6+} to metallic W^0 upon contact with sodium metal, thus leading to increased interfacial resistance and rapid battery degradation.[17] To address this issue, a common strategy involves constructing an interphase layer that is electronically

[a]Ningbo Institute of Materials Technology and Engineering, Chinese Academy of Sciences, Ningbo 315201, P. R. China. E-mail: liyong@nimte.ac.cn; yaoxy@nimte.ac.cn

[b]Center of Materials Science and Optoelectronics Engineering, University of Chinese Academy of Sciences, Beijing, 100049, P. R. China

[c]Nano Science and Technology Institute, University of Science and Technology of China, Suzhou 215123, P. R. China

insulating but ionically conductive through elemental doping. Such interphases effectively prevent direct contact between the solid electrolyte and sodium metal, thereby suppressing undesirable side reactions and promoting long-term cycling stability.[18–21] For instance, Wang *et al.* synthesized a W–B co-doped Na_3SbS_4 solid electrolyte where a Na–B compound interfacial layer was formed upon reaction with sodium metal. This interfacial layer allowed Na^+ transport while blocking electron transfer, effectively suppressing W^{6+} reduction and mitigating interfacial degradation. Consequently, the Na/$Na_3Sb_{0.95}W_{0.05}S_{3.95}B_{0.05}$/Na symmetric cell achieved durable operation over 500 h under 0.05 mA cm^{-2}.[22] Similarly, Meng *et al.* systematically investigated the properties of the interface between metallic sodium and a Cl-doped Na_3PS_4 solid electrolyte through X-ray photoelectron spectroscopy (XPS), and identified NaCl and S–P–Cl compounds within the solid electrolyte interphase (SEI) layer formed at the electrolyte/sodium interface. This SEI layer effectively reduces the electronic conductivity at the interface, thereby inhibiting electrolyte decomposition and improving interfacial stability. The assembled TiS_2/$Na_{2.9375}PS_{3.9375}Cl_{0.0625}$/Na cell maintained a discharge capacity of 80 mAh g^{-1} after 10 cycles at a current density of 0.149 mA cm^{-2}.[23] Inspired by these doping strategies, a W and Cl co-doping approach was proposed to optimize Na_3SbS_4 due to the similar ionic radii of W^{6+} (60 pm) and Sb^{5+} (60 pm), and Cl^- (181 pm) and S^{2-} (184 pm),[24] thereby ensuring minimal strain and preserving a tetragonal framework after structural substitution. Furthermore, the lower charge density of Cl^- compared to S^{2-} weakens the electrostatic interaction with mobile Na^+ ions, thereby lowering the migration energy barrier. Therefore, it is anticipated that aliovalent co-doping of W^{6+} and Cl^- into Na_3SbS_4 could yield a solid electrolyte exhibiting both enhanced ionic conductivity and improved interfacial stability toward sodium metal.

In this work, $Na_{2.95-x}Sb_{0.95}W_{0.05}S_{4-x}Cl_x$ ($x = 0$, 0.05, 0.1, 0.15, 0.2) was prepared through melt-quenching followed by an annealing process. Based on the charge compensation mechanism, Na vacancies can be introduced by the substitution of Sb^{5+} with W^{6+} and S^{2-} with Cl^-. The optimized $Na_{2.85}Sb_{0.95}W_{0.05}S_{3.9}Cl_{0.1}$ exhibits a room-temperature ionic conductivity of 12.66 mS cm^{-1}, significantly surpassing that of Na_3SbS_4 of 0.92 mS cm^{-1}. The incorporation of Cl leads to the *in situ* formation of an electronically insulating NaCl interfacial layer between the solid electrolyte and sodium metal, which effectively suppresses interfacial side reactions and enhances interfacial stability. The Na/$Na_{2.85}Sb_{0.95}W_{0.05}S_{3.9}Cl_{0.1}$/Na symmetric cell demonstrates stable cycling over 800 h. Furthermore, the TiS_2/$Na_{2.85}Sb_{0.95}W_{0.05}S_{3.9}Cl_{0.1}$/Na ASSSB exhibits an initial charge capacity of 142.2 mAh g^{-1} at 0.1C, maintaining 81.6% of this capacity after 100 cycles.

2. Results and discussion

The Na_3SbS_4 and $Na_{3-x}Sb_{1-x}W_xS_4$ ($x = 0$, 0.025, 0.05, 0.075, and 0.1) solid electrolytes were synthesized *via* a melt-quenching and annealing method. The optimized $Na_{2.95}Sb_{0.95}W_{0.05}S_4$ electrolyte demonstrates an ionic conductivity of 10.02 mS cm^{-1}, which represents a tenfold increase compared to the 0.92 mS cm^{-1} observed in pristine Na_3SbS_4 (Fig. S1 and Table S1).[15,25] Based on the $Na_{2.95}Sb_{0.95}W_{0.05}S_4$ solid electrolyte, the W–Cl co-doped $Na_{2.95-x}Sb_{0.95}W_{0.05}S_{4-x}Cl_x$ (x = 0.05, 0.1, 0.15, and 0.2) solid electrolyte was synthesized. The X-ray diffraction

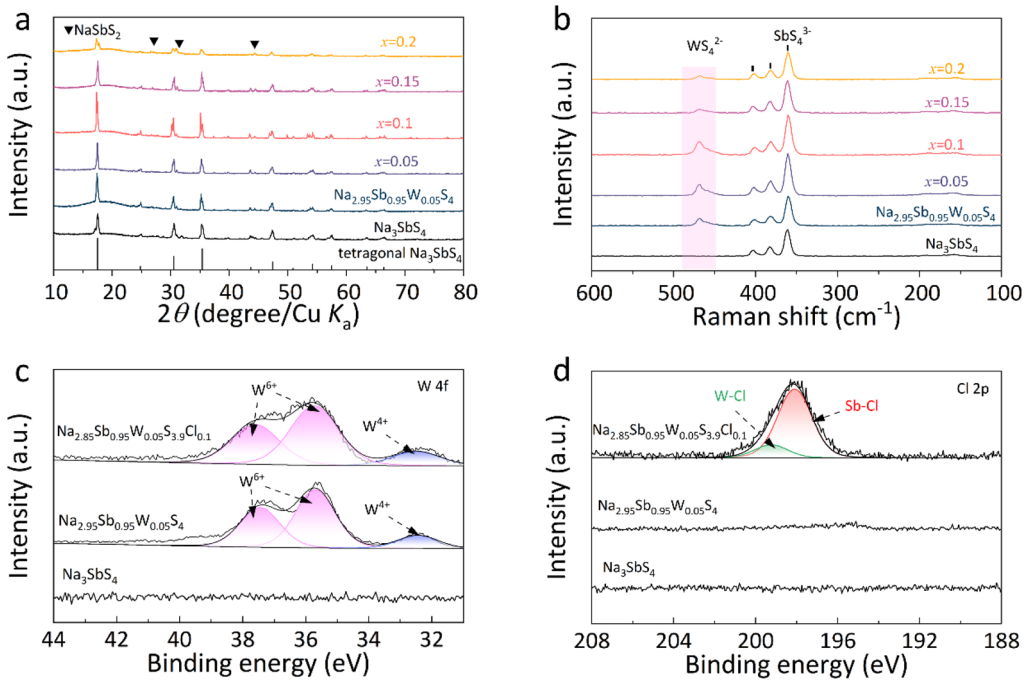

Fig. 1 (a) XRD patterns and (b) Raman spectra of Na_3SbS_4, $Na_{2.95}Sb_{0.95}W_{0.05}S_4$ and $Na_{2.95-x}Sb_{0.95}W_{0.05}S_{4-x}Cl_x$ (x = 0.05, 0.1, 0.15, and 0.2) solid electrolytes; (c) W 4f and (d) Cl 2p XPS spectra of Na_3SbS_4, $Na_{2.95}Sb_{0.95}W_{0.05}S_4$, and $Na_{2.85}Sb_{0.95}W_{0.05}S_{3.9}Cl_{0.1}$ solid electrolytes.

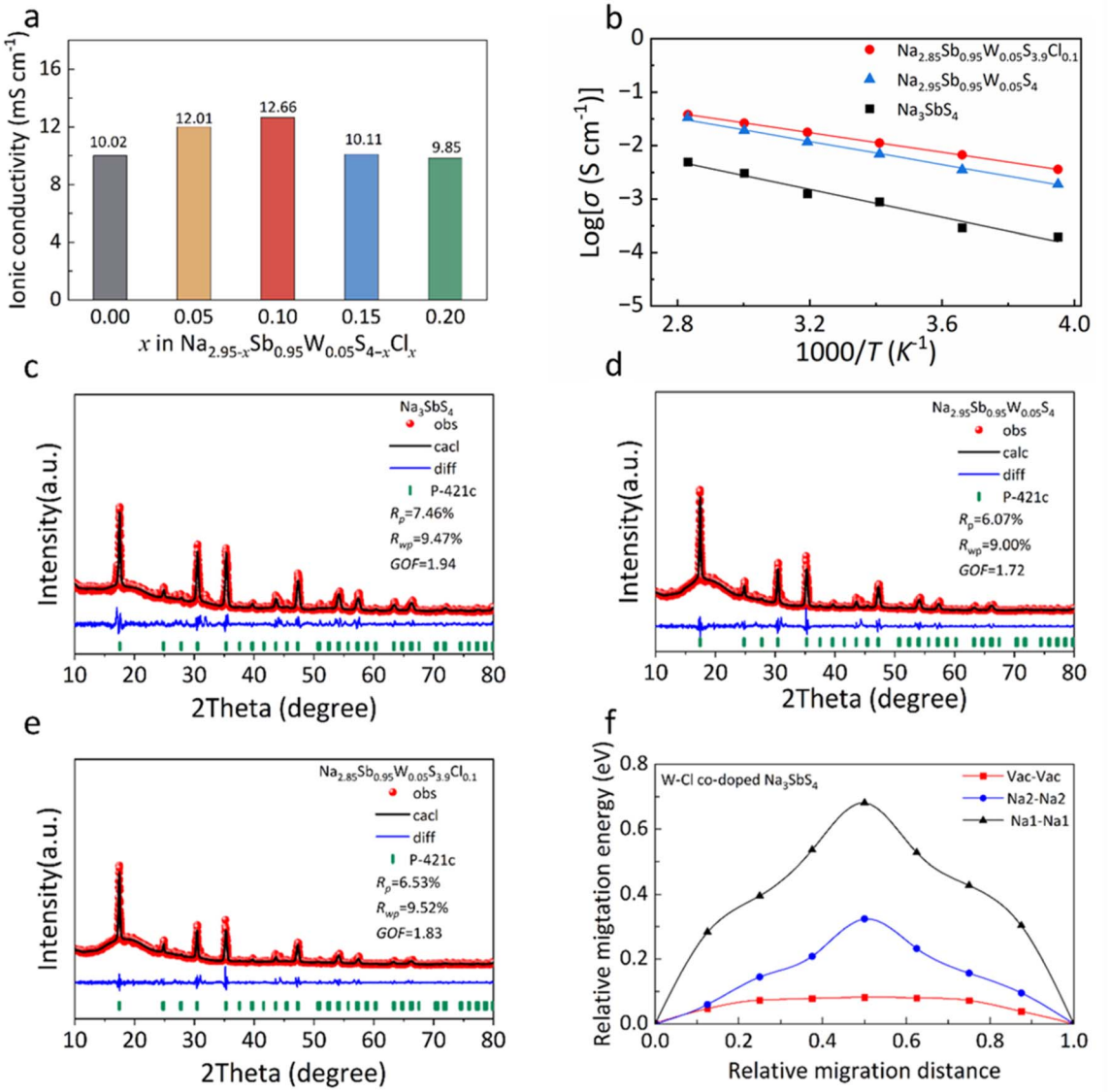

Fig. 2 (a) Ionic conductivities of $Na_{2.95-x}Sb_{0.95}W_{0.05}S_{4-x}Cl_x$ (x = 0, 0.05, 0.1, 0.15, and 0.2) solid electrolytes; (b) Arrhenius plots of Na_3SbS_4, $Na_{2.95}Sb_{0.95}W_{0.05}S_4$, and $Na_{2.85}Sb_{0.95}W_{0.05}S_{3.9}Cl_{0.1}$ solid electrolytes; Rietveld refinements of XRD patterns for (c) Na_3SbS_4, (d) $Na_{2.95}Sb_{0.95}W_{0.05}S_4$ and (e) $Na_{2.85}Sb_{0.95}W_{0.05}S_{3.9}Cl_{0.1}$; and (f) relative migration energy profiles of Na^+ in W–Cl co-doped Na_3SbS_4 along three typical migration pathways: Na1–Na1, Na2–Na2 and Vac–Vac.

(XRD) patterns of Na_3SbS_4, $Na_{2.95}Sb_{0.95}W_{0.05}S_4$, and $Na_{2.95-x}Sb_{0.95}W_{0.05}S_{4-x}Cl_x$ (x = 0.05, 0.1, 0.15, and 0.2) are shown in Fig. 1a. The peak splitting at 30.2° and 35.1° in Na_3SbS_4 confirms its tetragonal structure,[26] and all doped solid electrolytes maintain the same structure. Owing to the identical ionic radii of W^{6+} and Sb^{5+}, and similar ionic radii of Cl^- and S^{2-}, the W–Cl co-doped Na_3SbS_4 exhibits no discernible shift in peak position.[16] Notably, the absence of NaCl peaks in $Na_{2.85}Sb_{0.95}W_{0.05}S_{3.9}Cl_{0.1}$ confirms successful Cl^- doping.

Raman spectroscopy was further employed to analyze the structures of the were electrolytes (Fig. 1b). Characteristic peaks at approximately 360, 380, and 410 cm^{-1} are observed in all the solid electrolytes, corresponding to the SbS_4^{3-} units. In $Na_{2.95}Sb_{0.95}W_{0.05}S_4$ and $Na_{2.95-x}Sb_{0.95}W_{0.05}S_{4-x}Cl_x$ (x = 0.05, 0.1, 0.15, and 0.2), an additional peak appeared at 470 cm^{-1}, corresponding to the formation of WS_4^{2-} units, indicating that W^{6+} successfully substituted Sb^{5+} in these solid electrolytes.[15,27] XPS was employed to conduct a detailed analysis of the chemical bonding and valence states of the elements in $Na_{2.95}Sb_{0.95}W_{0.05}S_4$ and $Na_{2.85}Sb_{0.95}W_{0.05}S_{3.9}Cl_{0.1}$. In both solid electrolytes, W^{6+} is identified as the dominant valence state (Fig. 1c), which is consistent with the formation of WS_4^{2-} units, indicating successful W doping in the solid electrolytes.[22,28] The Cl 2p XPS spectrum of $Na_{2.85}Sb_{0.95}W_{0.05}S_{3.9}Cl_{0.1}$ (Fig. 1d) exhibits two peaks at 198.2 eV and 199.1 eV, corresponding to Sb–Cl and W–Cl bonds, respectively.[29,30] No characteristic peak of NaCl was observed, indicating that Cl had successfully substituted for S in the solid electrolyte. Collectively, the XRD, Raman and XPS results demonstrate the successful synthesis of

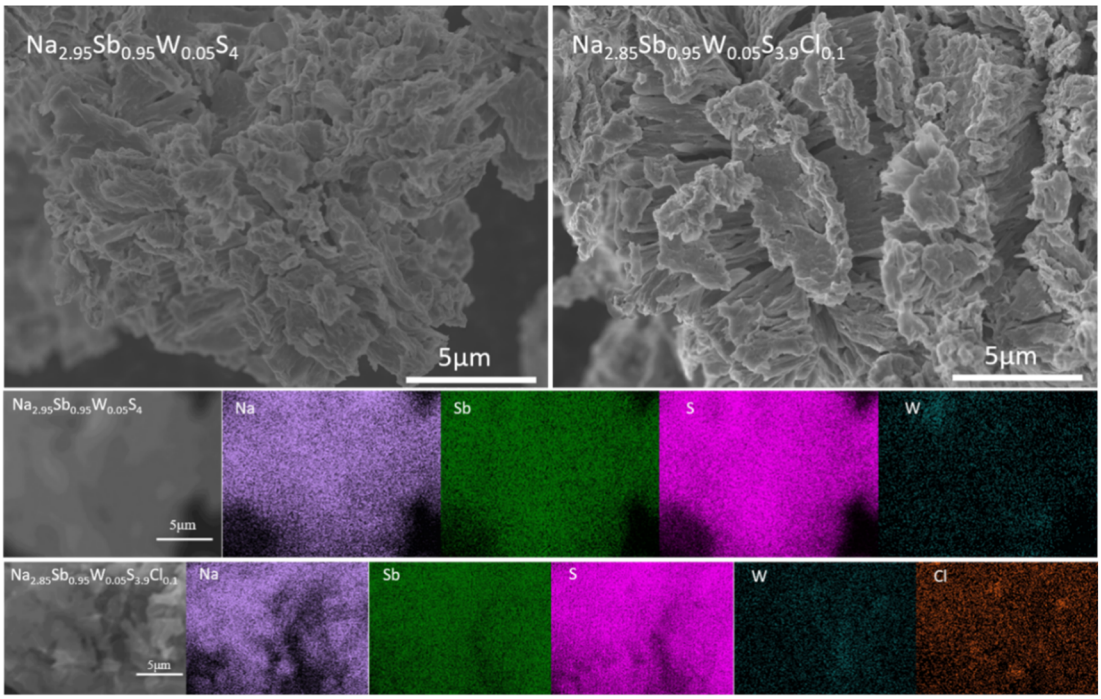

Fig. 3 SEM images and corresponding elemental mapping images of $Na_{2.95}Sb_{0.95}W_{0.05}S_4$ and $Na_{2.85}Sb_{0.95}W_{0.05}S_{3.9}Cl_{0.1}$ powders.

the W–Cl co-doped tetragonal Na_3SbS_4 solid electrolyte by the melt-quenching approach.

For the W–Cl co-doped $Na_{2.95-x}Sb_{0.95}W_{0.05}S_{4-x}Cl_x$ (x = 0, 0.05, 0.1, 0.15, and 0.2) solid electrolytes, the incorporation of Cl^- leads to a further enhancement in ionic conductivity compared to the solely W-doped composition. When x = 0.1, $Na_{2.85}Sb_{0.95}W_{0.05}S_{3.9}Cl_{0.1}$ exhibits an ionic conductivity of 12.66 mS cm^{-1} (Fig. 2a and Table S2). The effects of W doping and W–Cl co-doping on the activation energy were further compared (Fig. 2b and S2). It can be observed that Na_3SbS_4 exhibits an activation energy of 0.26 eV. After W doping, the activation energy decreases to 0.21 eV for $Na_{2.95}Sb_{0.95}W_{0.05}S_4$, and is further reduced to 0.18 eV for the W–Cl co-doped $Na_{2.85}Sb_{0.95}W_{0.05}S_{3.9}Cl_{0.1}$. This progressive reduction in the activation energy is consistent with the introduction of additional Na^+ vacancies induced by aliovalent W and Cl substitution, which facilitates Na^+ transport. In addition, as shown in Fig. S3, the W-doped sample exhibits a noticeably higher electronic conductivity of 3.56×10^{-8} S cm^{-1} than the Na_3SbS_4 with 4.64×10^{-9} S cm^{-1}, likely due to the variable valence of W, which introduces additional electronic states. Nevertheless, the incorporation of Cl effectively reduces the electronic conductivity to 2.16×10^{-8} S cm^{-1} due to the insulating nature of Cl, which could mitigate the risk of internal dendrite nucleation.[31]

Rietveld refinements were further performed on the XRD patterns of the solid electrolytes, *i.e.* Na_3SbS_4, $Na_{2.95}Sb_{0.95}W_{0.05}S_4$ and $Na_{2.85}Sb_{0.95}W_{0.05}S_{3.9}Cl_{0.1}$ (Fig. 2c–e). All three electrolytes have tetragonal crystal structures with the space group $P\bar{4}2_1c$. The refined lattice parameters and site occupancies of each element are listed in Tables S3–S5. In Na_3SbS_4, both the Na1 and Na2 sites are fully occupied with no Na^+ vacancies observed. In contrast, $Na_{2.95}Sb_{0.95}W_{0.05}S_4$ shows 95% occupancy at the Na2 sites, while $Na_{2.85}Sb_{0.95}W_{0.05}S_{3.9}Cl_{0.1}$ exhibits only 85% occupancy, indicating that W–Cl co-doping effectively increases the number of Na^+ vacancies within the Na_3SbS_4 framework.

To elucidate the correlation between vacancy concentration and enhanced ionic conductivity, density functional theory (DFT) calculations were performed to determine the energy profiles of three typical migration pathways in W–Cl co-doped Na_3SbS_4: Na1–Na1, Na2–Na2, and Vac–Vac (Fig. 2f). The calculated migration energy barriers are 0.68 eV (Na1–Na1), 0.32 eV (Na2–Na2), and 0.08 eV (Vac–Vac). These results indicate that the vacancy-mediated pathway requires the least energy, enabling more efficient Na^+ transport. Clearly, these findings demonstrate that W–Cl co-doping enhances ionic conductivity by increasing Na^+ vacancy concentration and reducing the diffusion energy barrier in Na_3SbS_4.[13]

Scanning electron microscopy (SEM) reveals similar microstructures among the Na_3SbS_4, $Na_{2.95}Sb_{0.95}W_{0.05}S_4$, and $Na_{2.85}Sb_{0.95}W_{0.05}S_{3.9}Cl_{0.1}$ solid electrolytes, indicating that the Cl doping does not induce significant morphological changes (Fig. 3 and S4). Energy-dispersive X-ray spectroscopy (EDS) reveals a homogeneous dispersion of the primary elements Na, Sb, and S as well as dopant elements W and Cl in the solid electrolytes, confirming the successful synthesis of the W–Cl co-doped Na_3SbS_4 solid electrolyte.

The chemical stability of the solid electrolyte in humid air was evaluated by measuring the H_2S released from the solid electrolyte at 45% humidity at 25 °C over a period of 120 min (Fig. 4). Na_3SbS_4 exhibited minimal H_2S release of only 0.07 cm^3 g^{-1}, whereas W doping the solid electrolyte significantly

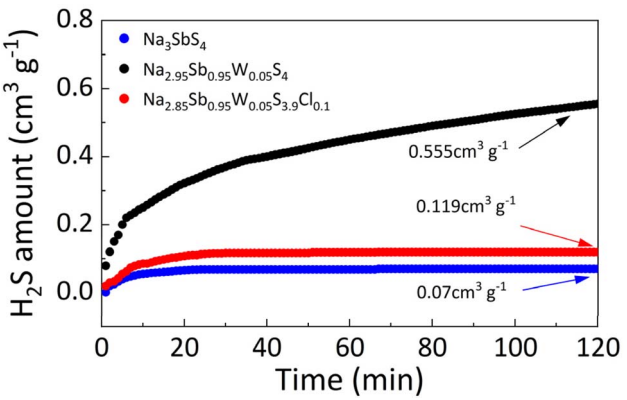

Fig. 4 Amount of H_2S gas generated in Na_3SbS_4, $Na_{2.95}Sb_{0.95}W_{0.05}S_4$ and $Na_{2.85}Sb_{0.95}W_{0.05}S_{3.9}Cl_{0.1}$ solid electrolytes at 45% air humidity at 25 °C.

increased the release to 0.555 $cm^3\ g^{-1}$, indicating greater susceptibility to moisture. In contrast, the W–Cl co-doped $Na_{2.85}Sb_{0.95}W_{0.05}S_{3.9}Cl_{0.1}$ exhibited a much lower H_2S release of 0.119 $cm^3\ g^{-1}$, demonstrating that Cl doping effectively improves moisture resistance and mitigates humidity-induced degradation.

In Na_3SbS_4 solid electrolytes, the SbS_4 units react with moisture in the air, resulting in the substitution of S by O and the release of H_2S gas.[32] Upon W doping, WS_4 units are formed in the $Na_{2.95}Sb_{0.95}W_{0.05}S_4$ solid electrolyte. With W–Cl co-doping, additional SbS_3Cl units are introduced in the $Na_{2.85}Sb_{0.95}W_{0.05}S_{3.9}Cl_{0.1}$ solid electrolyte (Fig. S5). To further elucidate the effect of W–Cl co-doping on the humid-air stability and structural integrity of Na_3SbS_4 electrolytes, the hydrolysis energies (ΔE_{hy}) of the main structural units (SbS_4, WS_4, and SbS_3Cl) in the three electrolytes were evaluated using DFT calculations. The calculated ΔE_{hy} values of the SbS_4, WS_4, and SbS_3Cl units are as follows (Table S6):

$$SbS_4 + H_2O \rightarrow SbS_3O + H_2S,\ \Delta E_{hy}\ (SbS_4) = 0.61\ eV$$

$$WS_4 + H_2O \rightarrow WS_3O + H_2S,\ \Delta E_{hy}\ (WS_4) = -0.07\ eV$$

$$SbS_3Cl + H_2O \rightarrow SbS_2OCl + H_2S,\ \Delta E_{hy}\ (SbS_3Cl) = 0.74\ eV$$

Compared with the SbS_4 units, the negative ΔE_{hy} value of WS_4 indicates that W doping facilitates the reaction between the solid electrolyte and moisture, leading to structural degradation and reduced humid-air stability. However, after Cl doping, the SbS_3Cl units exhibit a higher ΔE_{hy} than SbS_4, suggesting that Cl doping effectively suppresses hydrolysis and enhances the humid-air stability of the solid electrolyte.

The interfacial stability between the solid electrolytes and sodium metal was assessed by examining the polarization voltage of symmetric cells with Na_3SbS_4, $Na_{2.95}Sb_{0.95}W_{0.05}S_4$ and $Na_{2.85}Sb_{0.95}W_{0.05}S_{3.9}Cl_{0.1}$ (Fig. 5). A notable increase in the polarization voltage is observed for the Na/Na_3SbS_4/Na cell after 400 h of operation, primarily due to the solid electrolyte decomposition that generates Sb^0 and Na_2S.[33] These decomposition products reduce ion transportation at the interface, thereby leading to a progressive rise in polarization voltage until cell failure occurs. Upon W doping, the electrolyte undergoes accelerated decomposition accompanied by the formation of metallic W^0, resulting in severe instability at the interface. Consequently, the polarization voltage of the Na/$Na_{2.95}Sb_{0.95}W_{0.05}S_4$/Na cell rapidly increases after 280 h. In contrast, the Na/$Na_{2.85}Sb_{0.95}W_{0.05}S_{3.9}Cl_{0.1}$/Na cell maintains stable cycling over 800 h with a polarization voltage of ±0.79 V. These results demonstrate that Cl doping significantly improves the interfacial compatibility between the solid electrolyte and sodium metal.

To elucidate the mechanism underlying the enhanced interfacial stability, XPS analysis was performed to examine the elemental valence state and chemical bonding at the interface between Na and the solid electrolyte after cycling in symmetric

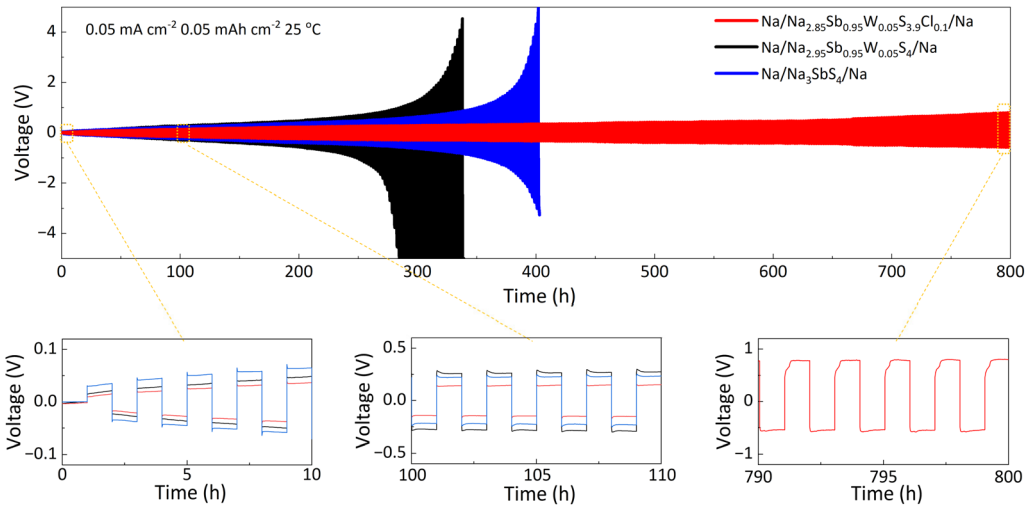

Fig. 5 Cyclic performances of Na//Na symmetrical cells using Na_3SbS_4, $Na_{2.95}Sb_{0.95}W_{0.05}S_4$ and $Na_{2.85}Sb_{0.95}W_{0.05}S_{3.9}Cl_{0.1}$ at 0.05 mA cm^{-2} and 0.05 mAh cm^{-2} at 25 °C.

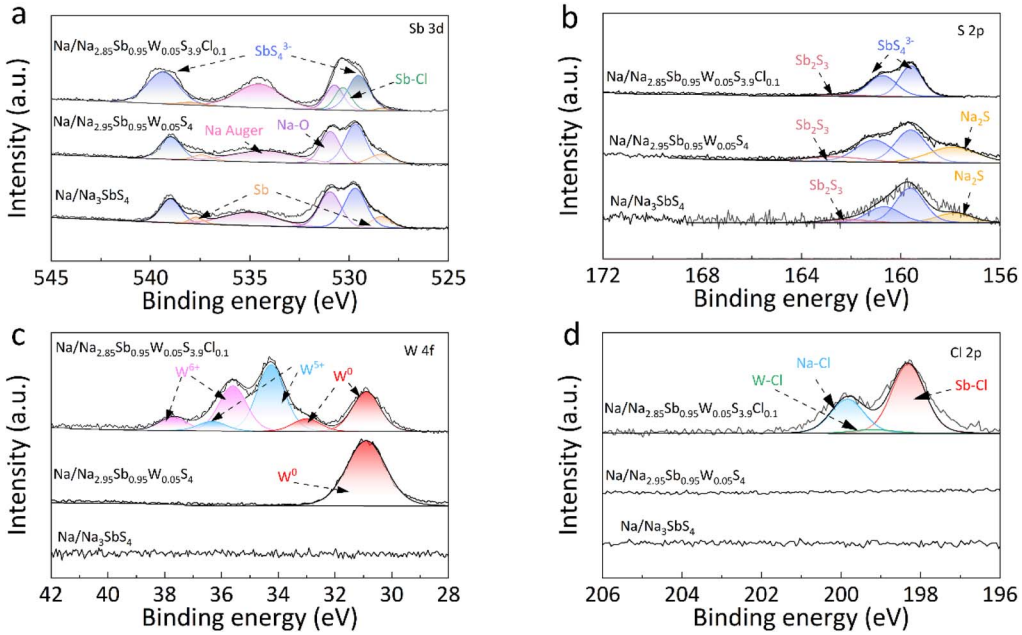

Fig. 6 XPS spectra of interfacial phases formed at Na metal and Na_3SbS_4, $Na_{2.95}Sb_{0.95}W_{0.05}S_4$ and $Na_{2.85}Sb_{0.95}W_{0.05}S_{3.9}Cl_{0.1}$ solid electrolytes after symmetric cell cycling: (a) Sb 3d; (b) S 2p; (c) W 4f; and (d) Cl 2p.

cells. At the Na/Na_3SbS_4 interface following cycling, the Sb 3d and S 2p spectra reveal the presence of SbS_4^{3-} units. However, partial reduction of Sb^{5+} to Sb^0 along with decomposition products, such as Sb_2S_3 and Na_2S, are also detected (Fig. 6a and b),[33,34] which indicates structural degradation of the Na_3SbS_4 solid electrolyte, thereby leading to increased interfacial resistance. At the Na/$Na_{2.95}Sb_{0.95}W_{0.05}S_4$ interface, the W 4f spectrum reveals only the W^0 signal, indicating complete reduction of W^{6+} to W^0 after cycling (Fig. 6c). This reduction is accompanied by continuous solid electrolyte decomposition and a corresponding increase in polarization voltage until cell failure. Simultaneously, XPS signals for Sb^0, Sb_2S_3, and Na_2S are also detected in the Sb 3d and S 2p spectra (Fig. 6a and b), confirming that both Na_3SbS_4 and $Na_{2.95}Sb_{0.95}W_{0.05}S_4$ undergo severe interfacial reactions with the sodium metal.

In contrast, at the Na/$Na_{2.85}Sb_{0.95}W_{0.05}S_{3.9}Cl_{0.1}$ interface, only weak signals of Sb^0 and Sb_2S_3 are observed in the Sb 3d and S 2p spectra, indicating that Cl doping effectively suppresses solid electrolyte decomposition induced by metallic sodium (Fig. 6a and b). Moreover, the W 4f spectrum can be deconvoluted into three oxidation states of W^0, W^{5+} and W^{6+}, with significantly reduced W^0 intensity (Fig. 6c),[35–38] which suggests that Cl doping also inhibits the reduction reactions of sodium metal with W species. The Cl 2p XPS spectrum of $Na_{2.85}Sb_{0.95}W_{0.05}S_{3.9}Cl_{0.1}$ after cycling shows peaks at 198.2 and 199.1 eV, corresponding to Sb–Cl and W–Cl bonds, respectively. In contrast to the results shown in Fig. 1d, a new peak at 199.7 eV corresponding to NaCl is detected,[39] indicating the generation of NaCl at the interface between sodium and the solid electrolyte (Fig. 6d). As an electronic insulator, NaCl can effectively suppress side reactions caused by electron leakage, thereby preventing the development of layers with mixed ionic/electronic conductivities.[18] The reduced W^0 and other decomposition products demonstrate that the NaCl layer mitigates both the reduction of W and the degradation of the solid electrolyte, ultimately enhancing the interfacial stability between the solid electrolyte and sodium metal. To explicitly demonstrate the superior comprehensive performance of the as-prepared electrolyte, a comparative analysis was conducted on the key metrics among recently reported high-performance sulfide electrolytes, as summarized in Table S7. Clearly, the $Na_{2.85}Sb_{0.95}W_{0.05}S_{3.9}Cl_{0.1}$ not only exhibits high ionic conductivity, but also maintains outstanding interfacial durability and robust air stability, thereby validating the effectiveness of the dual-doping and interface engineering strategy.

All-solid-state TiS_2/solid electrolyte/Na batteries were constructed and tested within a voltage range of 1.0–2.5 V (Fig. 7a, b, S6a, and c). The discharge/charge specific capacities of the TiS_2/Na_3SbS_4/Na, TiS_2/$Na_{2.95}Sb_{0.95}W_{0.05}S_4$/Na, and TiS_2/$Na_{2.85}Sb_{0.95}W_{0.05}S_{3.9}Cl_{0.1}$/Na batteries are 145.3/97.2, 226.4/141.2, and 250.3/142.2 mAh g^{-1} at 0.1C, respectively. The low ionic conductivity of Na_3SbS_4 limits the initial capacity of the all-solid-state TiS_2/Na_3SbS_4/Na battery. Meanwhile, the formation of W^0 at the Na/$Na_{2.95}Sb_{0.95}W_{0.05}S_4$ interface results in a continuous increase in interfacial impedance, leading to significant polarization in the TiS_2/$Na_{2.95}Sb_{0.95}W_{0.05}S_4$/Na battery and a capacity drop to only 5.1 mAh g^{-1} after 60 cycles. In contrast, benefiting from the enhanced ionic conductivity of the $Na_{2.85}Sb_{0.95}W_{0.05}S_{3.9}Cl_{0.1}$ electrolyte and the formation of a protective NaCl interfacial layer at the Na/solid electrolyte interface, the TiS_2/$Na_{2.85}Sb_{0.95}W_{0.05}S_{3.9}Cl_{0.1}$/Na battery demonstrates an improved initial charge capacity and significantly enhanced cycling stability with 81.6% of its initial capacity (116.1 mAh g^{-1}) after 100 cycles.

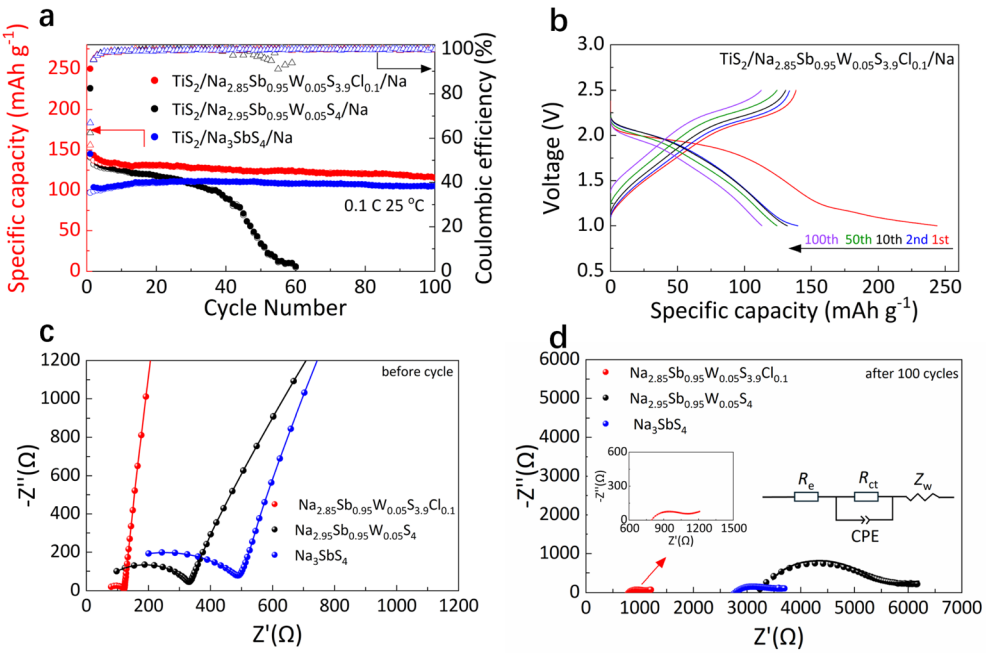

Fig. 7 (a) Cyclic performances of $TiS_2/Na_3SbS_4/Na$, $TiS_2/Na_{2.95}Sb_{0.95}W_{0.05}S_4/Na$ and $TiS_2/Na_{2.85}Sb_{0.95}W_{0.05}S_{3.9}Cl_{0.1}/Na$ at 0.1C between 1.0 and 2.5 V at 25 °C. (b) Charge/discharge profiles of the battery using $Na_{2.85}Sb_{0.95}W_{0.05}S_{3.9}Cl_{0.1}$ at 0.1C; Nyquist plots and equivalent circuit of the $TiS_2/Na_3SbS_4/Na$, $TiS_2/Na_{2.95}Sb_{0.95}W_{0.05}S_4/Na$, and $TiS_2/Na_{2.85}Sb_{0.95}W_{0.05}S_{3.9}Cl_{0.1}/Na$ batteries (c) before and (d) after cycling at 0.1C.

Electrochemical impedance spectroscopy (EIS) results for TiS_2/solid electrolyte/Na batteries before and after cycling at 0.1C are shown in Fig. 7c and d. In the equivalent circuit model, R_e represents the bulk resistance of both the electrodes and solid electrolyte, R_{ct} corresponds to the interfacial charge transfer resistance, the constant phase element (CPE) corresponds to the non-ideal double-layer capacitive behavior at the electrode–electrolyte interface, and Z_w represents the Warburg impedance, which is related to sodium ion diffusion into the bulk electrode. To accurately determine the individual resistance components, the EIS data were fitted using the equivalent circuit shown in the figures, and the corresponding fitted Nyquist plots are presented in Fig. S7, while the specific extracted values are listed in Table S8. For the $TiS_2/Na_3SbS_4/Na$

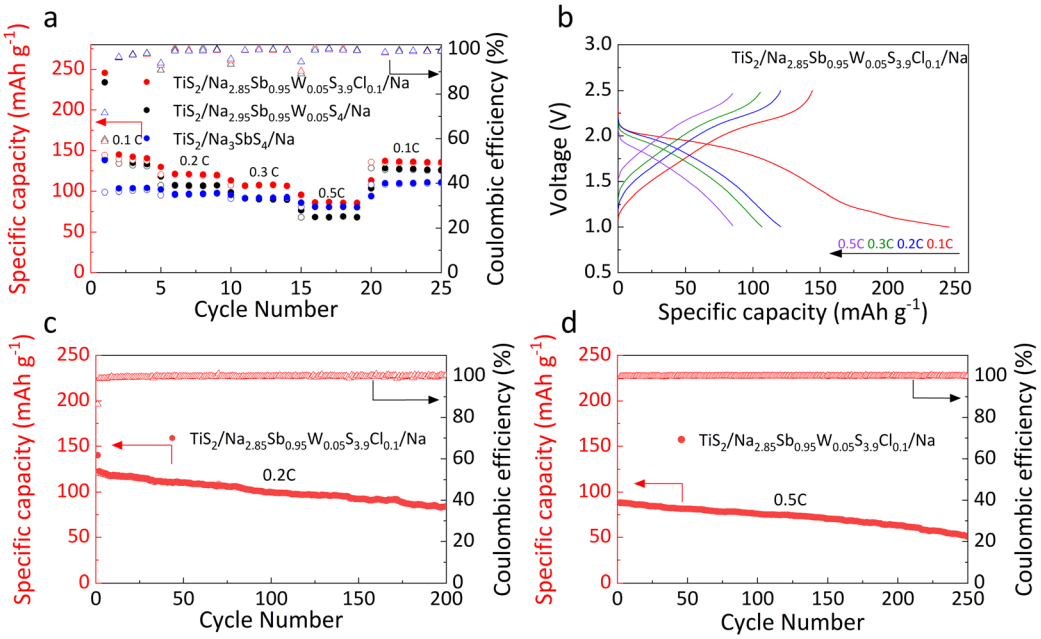

Fig. 8 (a) Rate capability of $TiS_2/Na_3SbS_4/Na$, $TiS_2/Na_{2.95}Sb_{0.95}W_{0.05}S_4/Na$ and $TiS_2/Na_{2.85}Sb_{0.95}W_{0.05}S_{3.9}Cl_{0.1}/Na$ batteries between 1.0 and 2.5 V at 25 °C. (b) Charge/discharge curves of $TiS_2/Na_{2.85}Sb_{0.95}W_{0.05}S_{3.9}Cl_{0.1}/Na$ from 0.1 to 0.5C. Cyclic performances of $TiS_2/Na_{2.85}Sb_{0.95}W_{0.05}S_{3.9}Cl_{0.1}/Na$ at (c) 0.2C and (d) 0.5C.

battery, interfacial reactions with sodium metal induce the solid electrolyte decomposition, leading to a substantial increase in R_e from 41.3 to 2786.6 Ω. Meanwhile, the decomposition products hinder ion transport across the interface, increasing R_{ct} from 441.5 to 615.4 Ω. In comparison, the $Na_{2.95}Sb_{0.95}W_{0.05}S_4$-based battery shows the most severe interfacial degradation, with R_e increasing from 69.1 Ω to 2872.2 Ω and R_{ct} increasing from 297.3 Ω to 2704.3 Ω. Furthermore, with Cl doping, the interfacial stability between $Na_{2.85}Sb_{0.95}W_{0.05}S_{3.9}Cl_{0.1}$ and the sodium metal is significantly improved, effectively mitigating both electrolyte decomposition and interface side reactions. Consequently, R_e only moderately increases from 76.8 Ω to 795.4 Ω, and the R_{ct} increases from 44.9 Ω to 316.2 Ω.

The rate capability was further evaluated at various current densities. Due to the low ionic conductivity of Na_3SbS_4, the TiS_2/Na_3SbS_4/Na battery exhibits relatively low reversible capacities of 98.8, 95.5, 91.6 and 81.0 mAh g^{-1} at 0.1, 0.2, 0.3 and 0.5C, respectively. After W doping, the TiS_2/$Na_{2.95}Sb_{0.95}W_{0.05}S_4$/Na battery shows reversible capacities of 139.4, 107.2, 91.9 and 68.3 mAh g^{-1} under identical charge–discharge rate conditions due to severe interfacial degradation between the solid electrolyte and metallic sodium (Fig. 8a, S6b and d). In contrast, W–Cl co-doping effectively enhances both the ionic conductivity and interfacial stability, resulting in significantly enhanced rate performance. The TiS_2/$Na_{2.85}Sb_{0.95}W_{0.05}S_{3.9}Cl_{0.1}$/Na battery delivers higher reversible capacities of 144.2, 120.4, 107.5 and 86.2 mAh g^{-1} at 0.1, 0.2, 0.3 and 0.5C, respectively (Fig. 8b). Upon returning to 0.1C, the capacity recovers to 135.8 mAh g^{-1} (Fig. 8a). Furthermore, the TiS_2/$Na_{2.85}Sb_{0.95}W_{0.05}S_{3.9}Cl_{0.1}$/Na battery retains 70.2% of its initial charge capacity after 200 cycles at 0.2C (Fig. 8c) and achieves stable cycling over 250 cycles at 0.5C (Fig. 8d).

3. Conclusions

Based on the principle of charge compensation, aliovalent co-doping of W^{6+} and Cl^- introduces sodium vacancies into the crystal lattice, thereby significantly enhancing the ionic conductivity of the solid electrolyte. Consequently, the $Na_{2.85}Sb_{0.95}W_{0.05}S_{3.9}Cl_{0.1}$ electrolyte demonstrates an ionic conductivity of 12.66 mS cm^{-1}, substantially higher than that of undoped Na_3SbS_4 of 0.92 mS cm^{-1}. The *in situ* formed electronically insulating NaCl interphase effectively suppresses the reduction of W and as well as the degradation of the solid electrolyte, thereby improving the interfacial stability between the solid electrolyte and sodium metal. As a result, the Na/$Na_{2.85}Sb_{0.95}W_{0.05}S_{3.9}Cl_{0.1}$/Na symmetric cell exhibited stable cycling performance over 800 hours at 0.05 mA cm^{-2}. Furthermore, the TiS_2/$Na_{2.85}Sb_{0.95}W_{0.05}S_{3.9}Cl_{0.1}$/Na battery delivered a specific charge capacity of 142.2 mAh g^{-1} at 0.1C and retained 81.6% of its initial charge capacity after 100 cycles. It also maintained 70.2% capacity retention after 200 cycles at 0.2C and demonstrated stable operation for over 250 cycles at 0.5C.

Conflicts of interest

There are no conflicts to declare.

Data availability

All data needed to evaluate the conclusions in this paper are present in the main manuscript or the supplementary information (SI). the SI includes experimental procedures, EIS measurements, SEM characterization, DFT computational details, and supplementary figures and tables. See DOI: https://doi.org/10.1039/d5sc09154c.

Acknowledgements

The work was supported by the Commanding Heights of Science and Technology of Chinese Academy of Sciences (Grant No. LDES150000), National Natural Science Foundation of China (Grant No. U21A2075, 52172253, 22309194, 52372244), Ningbo S&T Innovation 2025 Major Special Programme (Grant No. 2023Z106), Zhejiang Provincial Key R&D Program of China (Grant No. 2022C01072, 2024C01095), Jiangsu Provincial S&T Innovation Special Programme for carbon peak and carbon neutrality (Grant No. BE2022007), Baima Lake Laboratory Joint Funds of the Zhejiang Provincial Natural Science Foundation of China (LBMHD24E020001) and Youth Innovation Promotion Association CAS (Y2021080).

References

1 T. Liu, Y. Zhang, Z. Jiang, X. Zeng, J. Ji, Z. Li, X. Gao, M. Sun, Z. Lin, M. Ling, J. Zheng and C. Liang, Exploring competitive features of stationary sodium ion batteries for electrochemical energy storage, *Energy Environ. Sci.*, 2019, **12**(5), 1512–1533.
2 Z. Li, P. Liu, K. Zhu, Z. Zhang, Y. Si, Y. Wang and L. Jiao, Solid-State Electrolytes for Sodium Metal Batteries, *Energy Fuels*, 2021, **35**(11), 9063–9079.
3 P. K. Nayak, L. Yang, W. Brehm and P. Adelhelm, From Lithium-Ion to Sodium-Ion Batteries: Advantages, Challenges, and Surprises, *Angew. Chem., Int. Ed.*, 2018, **57**(1), 102–120.
4 W. Hou, X. Guo, X. Shen, K. Amine, H. Yu and J. Lu, Solid electrolytes and interfaces in all-solid-state sodium batteries: Progress and perspective, *Nano Energy*, 2018, **52**, 279–291.
5 C. Zhao, L. Liu, X. Qi, Y. Lu, F. Wu, J. Zhao, Y. Yu, Y.-S. Hu and L. Chen, Solid-State Sodium Batteries, *Adv. Energy Mater.*, 2018, **8**(17), 1703012.
6 H. Ahmad, K. T. Kubra, A. Butt, U. Nisar, F. J. Iftikhar and G. Ali, Recent progress, challenges, and perspectives in the development of solid-state electrolytes for sodium batteries, *J. Power Sources*, 2023, **581**, 233518.
7 Y. Qiu and J. Xu, Challenges and prospects for room temperature solid-state sodium-sulfur batteries, *Nano Res.*, 2024, **17**(3), 1402–1426.
8 A. Banerjee, K. H. Park, J. W. Heo, Y. J. Nam, C. K. Moon, S. M. Oh, S.-T. Hong and Y. S. Jung, Na_3SbS_4: A Solution Processable Sodium Superionic Conductor for All-Solid-State Sodium-Ion Batteries, *Angew. Chem., Int. Ed.*, 2016, **55**(33), 9634–9638.
9 S. Zhao, H. Che, S. Chen, H. Tao, J. Liao, X.-Z. Liao and Z.-F. Ma, Research Progress on the Solid Electrolyte of Solid-State Sodium-Ion Batteries, *Electrochem. Energy Rev.*, 2024, **7**(1), 3.

10 X. Guo, S. Halacoglu, Y. Chen and H. Wang, Recent Progress on Dominant Sulfide-Type Solid-State Na Superionic Conductors for Solid-State Sodium Batteries, *Small*, 2024, **20**(33), 2311195.
11 W. D. Richards, T. Tsujimura, L. J. Miara, Y. Wang, J. C. Kim, S. P. Ong, I. Uechi, N. Suzuki and G. Ceder, Design and synthesis of the superionic conductor Na10SnP2S12, *Nat. Commun.*, 2016, **7**(1), 11009.
12 A. Hayashi, K. Noi, A. Sakuda and M. Tatsumisago, Superionic glass-ceramic electrolytes for room-temperature rechargeable sodium batteries, *Nat. Commun.*, 2012, **3**(1), 856.
13 L. Zhang, D. Zhang, K. Yang, X. Yan, L. Wang, J. Mi, B. Xu and Y. Li, Vacancy-Contained Tetragonal Na_3SbS_4 Superionic Conductor, *Adv. Sci.*, 2016, **3**(10), 1600089.
14 F. Tsuji, N. Masuzawa, A. Sakuda, M. Tatsumisago and A. Hayashi, Preparation and Characterization of Cation-Substituted Na_3SbS_4 Solid Electrolytes, *ACS Appl. Energy Mater.*, 2020, **3**(12), 11706–11712.
15 A. Hayashi, N. Masuzawa, S. Yubuchi, F. Tsuji, C. Hotehama, A. Sakuda and M. Tatsumisago, A sodium-ion sulfide solid electrolyte with unprecedented conductivity at room temperature, *Nat. Commun.*, 2019, **10**(1), 5266.
16 W. Weng, G. Liu, Y. Li, L. Shen and X. Yao, Tungsten and oxygen co-doped stable tetragonal phase Na_3SbS_4 with ultrahigh ionic conductivity for all-solid-state sodium batteries, *Appl. Mater. Today*, 2022, **27**, 101448.
17 S. Lou, F. Zhang, C. Fu, M. Chen, Y. Ma, G. Yin and J. Wang, Interface Issues and Challenges in All-Solid-State Batteries: Lithium, Sodium, and Beyond, *Adv. Mater.*, 2021, **33**(6), 2000721.
18 H. Cao, M. Yu, L. Zhang, Z. Zhang, X. Yan, P. Li and C. Yu, Stabilizing Na_3SbS_4/Na interface by rational design via Cl doping and aqueous processing, *J. Mater. Sci. Technol.*, 2021, **70**, 168–175.
19 H. Jia, L. Peng, C. Yu, L. Dong, S. Cheng and J. Xie, Chalcogenide-based inorganic sodium solid electrolytes, *J. Mater. Chem. A*, 2021, **9**(9), 5134–5148.
20 P. Hu, Y. Zhang, X. Chi, K. K. Rao, F. Hao, H. Dong, F. Guo, Y. Ren, L. C. Grabow and Y. Yao, Stabilizing the Interface between Sodium Metal Anode and Sulfide-Based Solid-State Electrolyte with an Electron-Blocking Interlayer, *ACS Appl. Mater. Interfaces*, 2019, **11**(10), 9672–9678.
21 S. Xiong, Z. Liu, L. Yang, Y. Ma, W. Xu, J. Bai and H. Chen, Anion and cation co-doping of Na_4SnS_4 as sodium superionic conductors, *Mater. Today Phys.*, 2020, **15**, 100281.
22 L. Wang, G. Liu, Y. Li, W. Weng, X. Xin and X. Yao, Tungsten and Boron Codoping toward High Ionic Conductivity and Stable Sodium Solid Electrolyte for All-Solid-State Sodium Batteries, *ACS Appl. Mater. Interfaces*, 2024, **16**(4), 4847–4853.
23 I.-H. Chu, C. S. Kompella, H. Nguyen, Z. Zhu, S. Hy, Z. Deng, Y. S. Meng and S. P. Ong, Room-Temperature All-solid-state Rechargeable Sodium-ion Batteries with a Cl-doped Na_3PS_4 Superionic Conductor, *Sci. Rep.*, 2016, **6**(1), 33733.
24 R. Shannon, Revised effective ionic radii and systematic studies of interatomic distances in halides and chalcogenides, *Acta Crystallogr., Sect. A*, 1976, **32**(5), 751–767.
25 X. Feng, H. Fang, P. Liu, N. Wu, E. C. Self, L. Yin, P. Wang, X. Li, P. Jena, J. Nanda and D. Mitlin, Heavily Tungsten-Doped Sodium Thioantimonate Solid-State Electrolytes with Exceptionally Low Activation Energy for Ionic Diffusion, *Angew. Chem., Int. Ed.*, 2021, **60**(50), 26158–26166.
26 H. Gamo, N. H. H. Phuc, H. Muto and A. Matsuda, Effects of Substituting S with Cl on the Structural and Electrochemical Characteristics of Na_3SbS_4 Solid Electrolytes, *ACS Appl. Energy Mater.*, 2021, **4**(6), 6125–6134.
27 S. Yubuchi, A. Ito, N. Masuzawa, A. Sakuda, A. Hayashi and M. Tatsumisago, Aqueous solution synthesis of Na_3SbS_4-Na_2WS_4 superionic conductors, *J. Mater. Chem. A*, 2020, **8**(4), 1947–1954.
28 A. Schellenberger, R. Schlaf, T. Mayer, E. Holub-Krappe, C. Pettenkofer, W. Jaegermann, U. A. Ditzinger and H. Neddermeyer, Na adsorption on the layered semiconductors SnS_2 and WSe_2, *Surf. Sci.*, 1991, **241**(3), L25–L29.
29 T. Birchall, J. A. Connor and I. H. Hillier, High-Energy Photoelectron Spectroscopy of Some Antimony Compounds, *J. Chem. Soc., Dalton Trans.*, 1975, (20), 2003–2006.
30 H.-M. Wu and S.-A. Chen, Dopant-polymer interaction: WCl_6-doped polyacetylene, *Synth. Met.*, 1987, **20**(2), 169–183.
31 Z. L. Dong, Y. Yuan, V. Martins, E. Jin, Y. Gan, X. Lin, Y. Gao, X. Hao, Y. Guan, J. Fu, X. Pang, Y. Huang, Q. H. Tu, T.-K. Sham and Y. Zhao, Structural insight and modulating of sulfide-based solid-state electrolyte for high-performance solid-state sodium sulfur batteries, *Nano Energy*, 2024, **128**, 109871.
32 Y. Zhu and Y. Mo, Materials Design Principles for Air-Stable Lithium/Sodium Solid Electrolytes, *Angew. Chem., Int. Ed.*, 2020, **59**(40), 17472–17476.
33 G. Xie, M. Tang, S. Xu, A. Brown and L. Sang, Degradation at the Na_3SbS_4/Anode Interface in an Operating All-Solid-State Sodium Battery, *ACS Appl. Mater. Interfaces*, 2022, **14**(43), 48705–48714.
34 L. Wang, D. Liu, G. Liu, H. Pan, L. Huang and X. Yao, Highly conductive $Na_{2.804}Sb_{0.879}W_{0.046}S_{3.7}F_{0.075}$ with moisture tolerance enables stable all-solid-state sodium batteries, *Nano Energy*, 2025, **142**, 111167.
35 T. Takei, XPS analysis of tungsten electrodeposit from formamide bath, *Mater. Lett.*, 1992, **13**(1), 56–63.
36 G. Vida, V. K. Josepovits, M. Győr and P. Deák, Characterization of Tungsten Surfaces by Simultaneous Work Function and Secondary Electron Emission Measurements, *Microsc. Microanal.*, 2003, **9**(4), 337–342.
37 K. T. Ng and D. M. Hercules, Studies of Nickel-Tungsten-Alumina Catalysts by X-ray Photoelectron Spectroscopy, *J. Phys. Chem.*, 1976, **80**(19), 2094–2102.
38 J. Yang, L. Li, C. Xiao and Y. Xie, Dual-Plasmon Resonance Coupling Promoting Directional Photosynthesis of Nitrate from Air, *Angew. Chem., Int. Ed.*, 2023, **62**(47), e202311911.
39 S. Kohiki, T. Ohmura and K. Kusao, Appraisal of a New Charge Correction Method in X-ray Photoelectron Spectroscopy, *J. Electron Spectrosc. Relat. Phenom.*, 1983, **31**(1), 85–90.